Combustion and Flame 233 (2021) 111614

Contents lists available at ScienceDirect

Combustion and Flame

journal homepage: www.elsevier.com/locate/combustflame

Obtaining pseudo-OH* radiation images from CFD solutions of transcritical flames

Federica Tonti[a,*], Jaka Perovšek[a,b], Jose' Zapata Usandivaras[a,c], Sebastian Karl[d], Justin S. Hardi[a], Youhi Morii[f], Michael Oschwald[a,e]

[a] DLR-Institute of Space Propulsion, Im Langen Grund, Hardthausen am Kocher 74239, Germany
[b] ZARM - Center of Applied Space Technology and Microgravity, Universität Bremen, Am Fallturm 2, Bremen 28359, Germany
[c] ISAE-SUPAERO, 10 Avenue Edouard Belin, Toulouse 31055, France
[d] DLR-Institute of Aerodynamics and Flow Technology, Bunsenstrasse 10, Göttingen 32073, Germany
[e] RWTH Aachen University, Institute of Jet Propulsion and Turbomachinery, Templergraben 55, Aachen 52062, Germany
[f] Institute of Fluid Science, Tohoku University, 2-1-1 Katahira, Aoba-ku, Sendai 980-8577, Japan

ARTICLE INFO

Article history:
Received 16 December 2020
Revised 13 July 2021
Accepted 14 July 2021

Keywords:
High-pressure combustion
CFD
Radiation modelling
Ray tracing
Flame emission

ABSTRACT

The quantitative comparison of experimental data and results from CFD simulations is still an ongoing challenge in the investigation of high pressure combustion in rocket combustion chambers. This is due to the extreme environment which develops in liquid propellant rocket engines, which represent a challenge for experimental data collection. OH* radiation emitted from the flame has often been designated as an indicator of the combustion zone, because of its relative ease of detection with appropriate cameras. A method was developed to compare OH* radiation originating from cryogenic oxygen-hydrogen flames in an experimental combustor with the CFD simulation results. Pseudo-OH* images were obtained from CFD results of two combustors. The method consists in obtaining the path of a ray of light by a reverse ray tracing algorithm and sampling the thermodynamic properties along the path of the ray, simulating the emission and absorption spectra in the wavelength range of interest, in this case of OH* emission during combustion. The spectral radiance is then determined by solving the differential radiative transfer equation. Finally, the total radiance is calculated integrating the spectral radiance. The results obtained applying this method are then compared with former results of two test cases, a laminar and a turbulent flame, and with the related experimental data. An improvement of the comparison with the experimental data was achieved in terms of the prediction of self-absorption, which was underestimated in previous works by a factor of 15, and in terms of radiance near the injection plane, where difference is estimated to be about 40% when including refraction. The method allows for more direct comparison between 3D CFD results and 2D experimental images collected by the optical setup and probes.

1. Introduction

High-pressure combustion as it appears in liquid propellant rocket engines is a challenge for the development of rocket combustion chambers. Numerical simulations are a promising tool for the development of new rocket engines. However, the extreme conditions in rocket combustion chambers is also challenging for combustion simulations. For that reason CFD simulations need to be validated against well instrumented experiments. The exact measurement of the physical properties of the flames has its own difficulties, especially for liquid propellant rocket engines (LPRE), due to the extreme conditions at which they operate. In particular, during combustion, very high temperatures and pressures are reached, and due to this unfriendly environment it is hard to obtain experimental data of important combustion parameters, for example mass fractions of the involved species or temperature.

A physical parameter which can be easily measured is the flame radiation, in particular the radiation emitted by excited hydroxyl radicals (OH*) when dealing with liquid oxygen/hydrogen flames. OH* radiation has been used already several times to identify flame emission zones in high temperature flames [1,2], being the most distinct radiation in flames in the UV range and it is often

---

[*] Corresponding author.
E-mail address: federica.tonti@dlr.de (F. Tonti).

https://doi.org/10.1016/j.combustflame.2021.111614

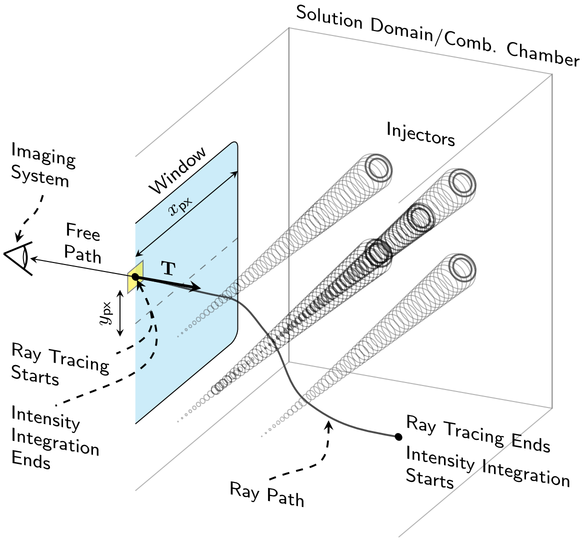

Fig. 1. Sketch of the ray tracing algorithm. The ray path starts on a point on the window, passes through the jets and reaches the chamber walls. On its path, emission and absorption spectra along the ray are calculated. When the ray reaches the chamber walls, the integration of the coefficient to obtain the intensity starts, ending at the window.

used as a marker of the flame because the central wavelength of its spectrum (310 nm) is clearly distinguishable from other (black body) sources. For example, at DLR Lampoldshausen OH* radiation was used to investigate combustion instabilities in experimental works by Hardi [3] and in a similar way at Purdue University [4]. At the Mascotte test bench, OH* radiation was recorded to provide flame visualization [5]. An extensive review on OH* radiation in flames is provided by Gaydon [6] and Mavrodineau [7]. Chemiluminescence originates from the relaxation of electronically excited species produced by the combustion reaction in the flame. Studying light emission taking place in the reaction zone provides information about the energy release in the flame radiation zone.

Several studies describe methodologies for comparison, mainly using chemiluminescence of excited radicals as a quantity for comparison relying on different chemical schemes to derive the radicals of interest from numerical simulations to be compared with experimental data. Early experimental studies used emissions of radicals as an indicator of the heat release rate in real combustion chambers and experimental combustors [8,9]. More recent studies have investigated the effect of varying some properties of flames on chemiluminescence [10–13]. Many fundamental research has been made to understand whether OH* radiation (and also CH* in hydrocarbon flames) could be an indicator of heat release [14–23] in order to define if a quantitative correlation between OH* radiation and heat release rate is possible. These studies assume that chemiluminescence takes place where the heat release rate is defined from chemical reactions. In these studies the degree of correlation between radical concentration and heat release rate depends strongly on physical variables including strain rate of the flame, degree of turbulence, degree of premixing, pressure and equivalence ratio.

However, most of the investigations involved hydrocarbon flames at low pressure and temperatures, whereas hydrogen high pressure and temperature flames have not been studied in detail. The temperature threshold at which the thermal excitation overcomes the chemical one was investigated and adjusted across the years, ranging from 2000 to 3000 K [24–27]. For relatively low temperature flames (below 2700 K at 50 bar pressure), chemical excitation overcomes thermal. Above 2700 K, thermal excitation becomes predominant and OH is assumed to be in thermal equilibrium with OH*. This is the main assumption of the Equilibrium Filtered Radiation Model (EFRM) developed by Fiala [28]. For high temperaure flames, Gardiner et al. [29] proposed a thermal excitation mechanism for OH* production, stating that collisions of OH ground-state molecules with third-body molecules have sufficient kinetic energy to exceed the energy threshold and form OH*. Experimentally, the relation between heat release and OH* radiation has not been investigated in detail for non-premixed O_2/H_2 flames. The only work is the one of Burrows [30], which used OH* radiation to determine the reaction zone.

A short discussion about the main challenges in measuring radiation from flames can be helpful to better understand why the topic is relevant. The measured total radiation consist of three main components: the flame radiation, which results from high

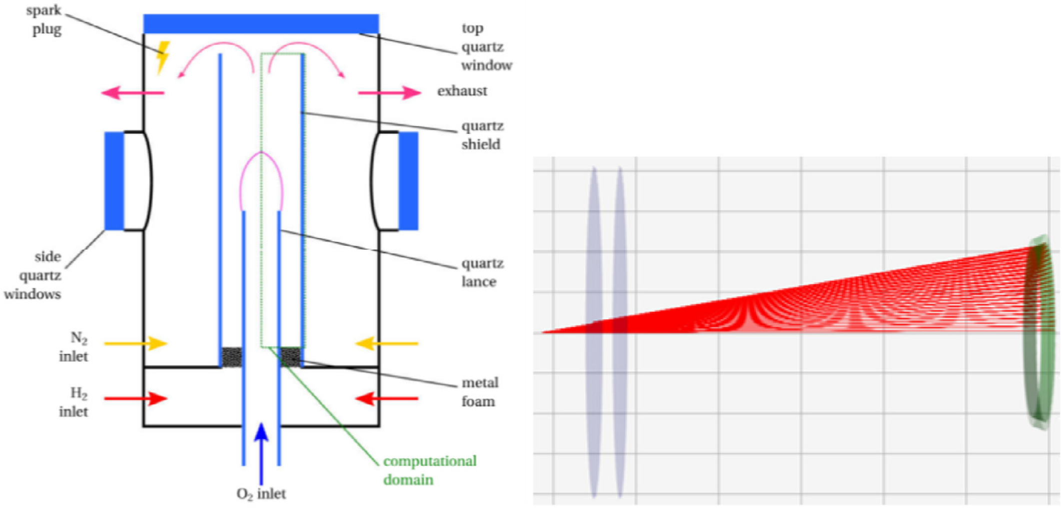

(a) Sketch of Fiala's experiment

(b) Sketch of the ray paths used in SMART.

Fig. 2. Sketch of the computational domain used for the simulations [28], and of the ray paths from the pinhole camera to the lens used in SMART. Figure 2b shows the path of rays colored in red between the pinhole camera (green area) and the quartz lenses. This is the path of the rays generated with SMART. The integration of the radiative equation is performed along these rays.

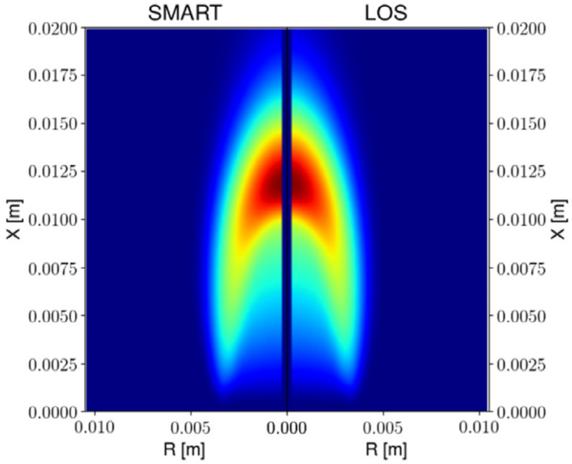

(a) 1 bar

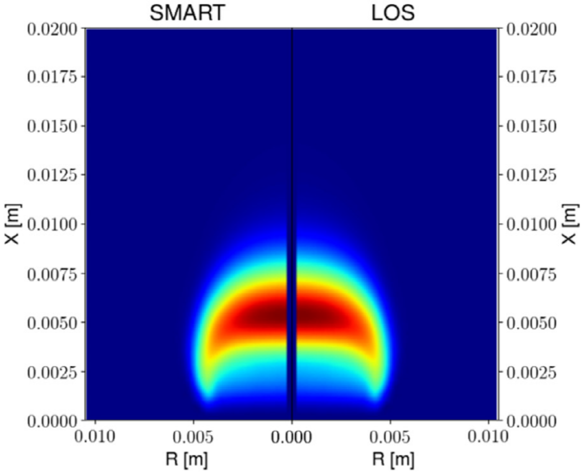

(b) 30 bar

Fig. 3. Comparison of SMART spectral modelling against integrated line of sight visualization for the laminar flame at 1 bar (a) and 30 bar (b). X represents the axial coordinate starting from the injection plane, R represents the radial coordinate of the domain. The radiance values are normalized between 0 (blue) and 1 (red). (For interpretation of the references to color in this figure legend, the reader is referred to the web version of this article.)

temperature combustion products and optically active gases, the radiation emitted from the walls of the chamber and the flame radiation reflected by the walls of the chamber. The radiation emitted and reflected from the walls is sometimes comparable or even greater than the flame radiation itself, especially when the wall temperature is high or the surface of the walls is highly reflective. In the current work the focus is on OH* radiation, with the use of filters to limit the collection of radiation to a narrow band in the UV range, the influence of the primarily infrared radiation from the chamber walls can be neglected.

Looking in detail to OH* measurement techniques, most of the studies are focused on chemiluminescence and measurements can provide only qualitative information. The chemiluminescent intensities can be converted to some extents into quantitative measurements using Raman and Rayleigh scattering techniques, but these become difficult to apply in practical rocket combustors. An alternative calibration technique for chemiluminescence of OH* was proposed by Zhao et al. [31]. This technique used a light source of known radiance to determine the local concentration of OH* radicals in a hydrogen diffusion flame. A recent work of Liu et al. [32] use the integration of a spherical and uniform light source to obtain the transformation of OH* and CH* from the light intensity to the emitting rate of a jet diffusion flame. In addition to the challenge in obtaining a quantitative measurement of radiation intensity, it is important to notice that the radiation itself is a physical quantity which is not directly associated with a specific thermodynamic property, therefore reducing the physical meaning of the measurement and leaving space for a number of physical interpretations.

CFD becomes then important in order to have insights in the physics of the flame radiation, also because it is not limited to line-of-sight measurements and giving quantitative estimates of the concentration of OH* in the flame zone. The wall radiation can be taken into account separately, clearly distinguishing it from the flame radiation itself. All these aspects can help also in reducing the costs associated to the experimental investigation.

A recent work of Sheikhani et al. [33] investigated the different factors affecting measurement and modeling of the flame radiation, focusing also on turbulence. In turbulent flames, the fluctuations of the velocity field enhance fluctuations of the species concentration and temperature field. These fluctuations influence in turn the radiation field because the emission of the radiation and the heat flux are non-linear functions of temperature and species concentration. On the other hand, temperature fluctuations induce radiative flux and velocity fluctuations, and therefore radiation modifies turbulence [34]. This phenomenon is named Turbulence-Radiation Interaction (TRI) [35]. In high turbulence combustion systems, taking into account the effects of radiation is crucial. There are several approaches to model flame radiation and therefore solve the Radiative Transfer Equation (RTE). When solving the equation directly, and assuming a homogeneous temperature, RTE can be solved without any other assumption on the thickness of the flame, and it can be considered as an absorption and emission model. This approach is known as optically thick flame model.

When the optical thickness tends to zero, the RTE can be simplified, and thus the solution of the equation, leading to the optically thin flame formulation, which can be considered as a limit case of RTE. The optically thin flame assumption is valid only if the intensity coming from the surroundings of the flame is very low as compared to the intensity supplied by the flame, but becomes wrong for example if the flame is attached to a hot surface or surrounded by an environment where the radiation from other sources is not negligible, for example by other identical flames like in a rocket combustion chamber. In particular, the optically thin flame assumption states that the radiation coming from the surroundings behind the flame and the inner of the flame is not attenuated, since self-absorption phenomena are ignored in this formulation. These approximations consider the flame as an emitting volume. However, in most industrial applications, solving the RTE in its original form is computationally expensive.

To save computational time, the flame can be considered as an emitting solid surface. In this context, the grey medium approximation is often used to model radiating systems. The term grey indicates a medium which is in thermal equilibrium, has an emissivity smaller than 1 and independent from the frequency. The grey medium model gives a huge advantage in terms of computational time. Usually, the spectral content of the considered problems shows if the grey medium approximation is acceptable or not. If a surface emits radiation at only one wavelength, then a grey model does not correctly describe the problem, because the grey surface emits radiation at all wavelengths. For cases where the emission bands are very few and very narrow a grey model will typically fail. On the other hand, if the radiation being considered is broadband then the grey medium approximation is useful.

Malalasekera et al. [36] show that methods based on ray-tracing techniques can be easily applied to temperature fluctuations when

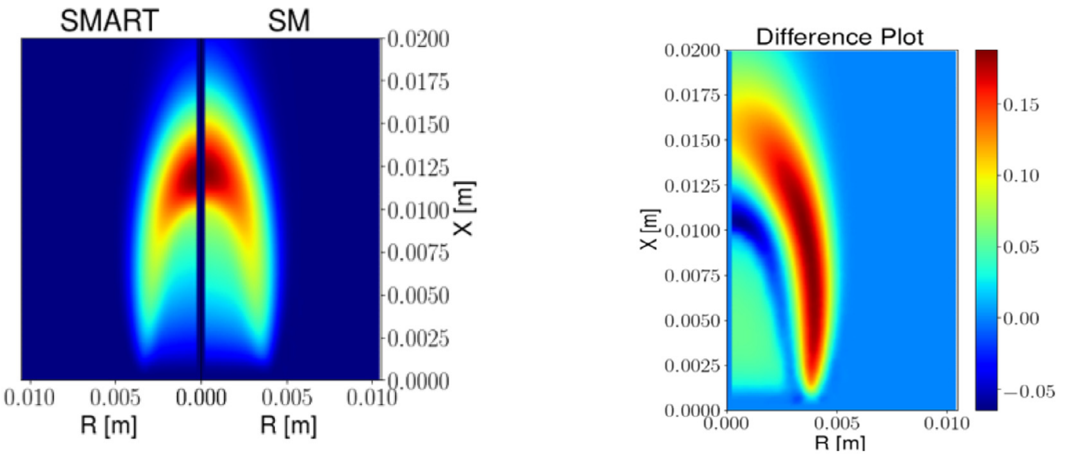

(a) Comparison of normalized OH* radiation

(b) Absolute difference plot of normalised OH* radiation

Fig. 4. Comparison of normalised OH* radiation between SMART and SM for a chamber pressure of 1 bar. The radiance values are normalized between 0 (blue) and 1 (red). Figure 4a shows the OH* radiation obtained with the application of the two models. Figure 4b shows the difference plot of the normalised OH* radiation obtained subtracting the radiance calculated with SMART to the radiance calculated with Fiala SM, showed in Fig. 4a. (For interpretation of the references to color in this figure legend, the reader is referred to the web version of this article.)

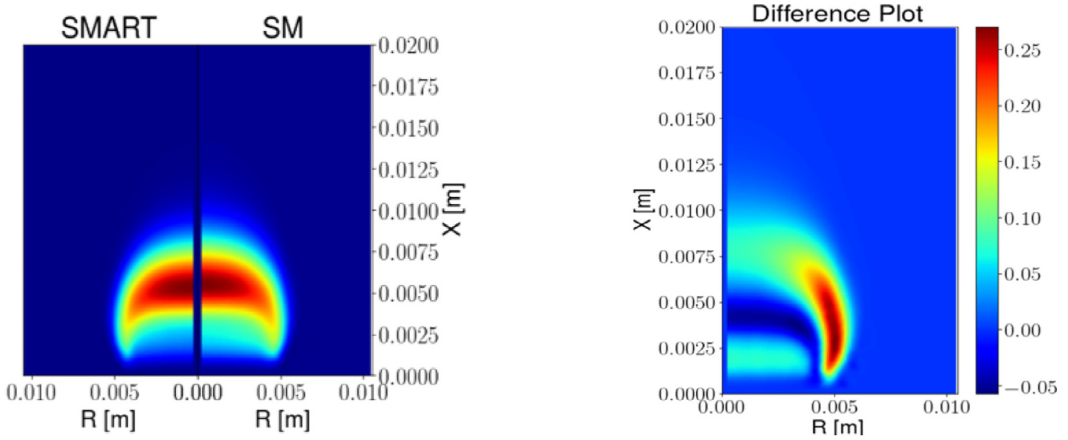

(a) Comparison of normalised OH* radiation

(b) Absolute difference plot of normalized OH* radiation

Fig. 5. Comparison of normalised OH* radiation between SMART and SM for a chamber pressure of 30 bar. The radiance values are normalized between 0 (blue) and 1 (red). Figure 5a shows the OH* radiation obtained with the application of the two models. Figure 5b shows the difference plot of the normalised OH* radiation obtained subtracting the radiance calculated with SMART to the radiance calculated with Fiala SM showed in Fig. 5a. (For interpretation of the references to color in this figure legend, the reader is referred to the web version of this article.)

using Probability Density Function (PDF) based combustion models. In the simulation domain considered by Malalasekera et al. [36], the grey-medium approximation gives larger errors than approximating the flame as optically thin. However, in the frame of OH* radiation, the assumption of optically thin flames yields considerable error, because self-absorption is not taken into account. The term self-absorption indicates that the radiation emitted from the molecules is subject to the absorption by the same molecules which are present in the ground state. Taking self-absorption into account is fundamental to model correctly the radiation of flames where OH is present as a combustion product in high concentrations. Previous studies underlined that self-absorption affects the flame radiation considerably with increasing pressures [28,37,38].

The work presented in this paper aims to take into account the fundamental phenomena which are involved in the radiative transport of OH* emission to reproduce images of the thermally excited OH radicals, in particular refraction and self-absorption which are the most important in non-premixed O_2/H_2 flames. Starting from RANS simulation results, the goal is to have a tool for comparison between experimental data and numerical simulations as a post-processing step, producing images of the OH* radiation generated by the excited OH radicals which are products of the combustion of O_2 and H_2. These images are pseudo-OH* images because OH* production is not modeled in the chemical reaction mechanism in order to reduce the computational effort of solving an additional equations for the chemistry reaction mechanisms at run time. In order to obtain the pseudo-OH* images, a radiation model of OH* is implemented, and a reverse ray-tracing algorithm is used in order to model the ray paths from the walls of an experimental combustor to the detector, passing through the flame and refracting where density gradients are encountered.

Section 2 describes the model used in this work together with the ray tracing algorithm used for visualization of the OH* radiation. In Section 3 the application of the method to an existing test case from Fiala [28] is presented, in order the compare the results of the algorithm developed in the frame of this work with results obtained with the pre-existing spectral model used by Fiala. Section 4 introduces an experimental test case with optical access from our group (Webster et al. [39]) considered for the application of the algorithm. Section 4.1 describes the numerical modeling in detail along with the results of the experimental test case, describing the data extracted from simulations and the comparison with the experimental data and previous simulations. Section 4.3 give space to discussion of the results. Section 5 introduces LES simulation results of the optically accessible rocket combustor obtained by Morii et al. [40]. The algorithm is then applied to the CFD simulation and results are discussed. Section 6 summarizes the results and presents conclusions and outlook.

2. The SMART algorithm

An algorithm to take self- absorption and refraction phenomena into account in the combustion chamber has been developed, named SMART (Spectral Model and Ray-Tracing). The algorithm is described in detail by Perovšek [41]. The calculations are spectrally resolved in a range of wavelengths from 305 nm to 320 nm, which accounts for self-absorption phenomena for OH, but the range of wavelengths can easily be extended by changing the settings for the radiation model. Diffraction, dispersion, scattering and blackbody radiation from walls and gases are neglected. In particular, diffraction can be neglected because of the nature of the investigated flames. In the first test case, the investigated flame is a laminar gas/gas flame, where no liquid particles are present and so no relevant diffraction due to these can take place. The second test case is an experimental combustor where LOx is injected and then heated up rapidly, so that both pressure and temperature are above the corresponding critical values. Due to the negligible surface tension no droplets of liquid oxygen are present and this phenomenon has no relevance. However, when dealing with subcritical injection conditions, the effect of diffraction should be considered. Refraction is taken into account based on the work of Smith [42], in which a ray-tracing technique applicable for both continuously varying and discrete refractive index boundaries in inhomogeneous media is developed. The input data of the algorithm is a solution from the CFD simulations and is represented by the nodes in an unstructured grid, with the physical properties evaluated at the nodes. The algorithm treats the input data as a quasi-continuum by using an inverse distance interpolation based on nearest neighbours.

A necessary pre-processing step for the simulation of refraction is the calculation of the refractive index n for each node in the input data. The refractive index is estimated by using the Gladstone-Dale relation [43]:

$$n(T,p) = 1 + \rho(T,p)\cdot k \tag{1}$$

where T denotes the temperature, p the pressure, ρ the density and k the Gladstone-Dale coefficient. For mixtures of fluids with different atomic and molecular species the representative Gladstone-Dale coefficient

$\bar{k} = \sum k_i \cdot x_i$ is used where k_i is the Gladstone-Dale coefficient of the species i and x_i the molar fraction of the species (at the evaluated point).

The first step in obtaining the pseudo-OH* images is the definition of the points at which the rays are expected to enter a detector by the position vector $\mathbf{r} = [r_x, r_y, r_z]^{\mathrm{T}}$ and the unit vector $\mathbf{T} = [T_x, T_y, T_z]^{\mathrm{T}}$ which correspond to the opposite direction of the light that would enter a detector. Each ray is then obtained by integrating the eikonal equation, which describes the electromagnetic wave propagation on a path s under the assumption of geometrical optics in a scalar field $n(\mathbf{r})$ of continuously changing refractive index n [44].

$$\frac{\mathrm{d}}{\mathrm{d}s}\left[n(\mathbf{r})\frac{\mathrm{d}\mathbf{r}}{\mathrm{d}s}\right] = \nabla n(\mathbf{r}) \tag{2}$$

This equation is split into two first order differential equations and solved with an explicit Runge-Kutta method of order 5 [45].

$$\frac{\mathrm{d}\mathbf{r}}{\mathrm{d}s} = \frac{\mathbf{T}}{n(\mathbf{r})} \tag{3}$$

$$\frac{\mathrm{d}\mathbf{T}}{\mathrm{d}s} = \nabla n(\mathbf{r}) \tag{4}$$

Points $\mathbf{r}$ and vector $\mathbf{T}$ are parts of the vector of initial conditions y_0 which are required by the solver:

$$y_0 = \begin{bmatrix} \mathbf{r}|_{s=0} \\ \frac{\mathbf{T}}{n}\big|_{s=0} \end{bmatrix} = \begin{bmatrix} r_x|_{s=0} \\ r_y|_{s=0} \\ r_z|_{s=0} \\ T_x/n|_{s=0} \\ T_y/n|_{s=0} \\ T_z/n|_{s=0} \end{bmatrix} \tag{5}$$

The solver stops as soon as the calculated position vector $\mathbf{r}(s)$ is outside of defined geometry boundaries and then outputs a solution set of vectors $[\mathbf{r}(s=0)\ldots\mathbf{r}(s=s_{\mathrm{end}})]^{\mathrm{T}}$ that represent the points on the ray.

Once the ray solution is available the thermodynamic properties (temperature T, pressure p and a set of mass fractions $X = [w_{H_2}, w_{H_2O}, w_{O_2}, w_{OH}]$) at any point along the ray can be interpolated with the help of the nearest neighbour interpolation routine. The mass fractions of H and O species are neglected as they are close to zero. The rest of the constituent mass fractions besides the OH mass fraction are scaled equally in order to make the sum of all considered mass fractions equal to 1.[1] The aforementioned properties are the inputs for a routine that determines the emission spectrum e_λ and absorption spectrum κ_λ.

OH* is not modeled as a separate species in the CFD calculations that provide the input dataset for the procedure explained in this work. In SMART the spectral modelling program by Potter is used [46] and adapted for the purposes of the OH* radiation modelling. In the radiation modelling program it is assumed that the OH* is in thermal equilibrium with the ground state OH, so the needed inputs are the mass fraction of OH, w_{OH}, temperature T and pressure p. The mass fractions w_i of other species i in the combustion chamber are provided to accurately simulate the molecular kinetics. For the emission and absorption spectra simulation, the assumption of local thermal equilibrium is made, which presumes equality between translational, rotational, vibrational and electronic temperature.

$$T = T_{Trans.} = T_{Rot.} = T_{Vib.} = T_{El.} \tag{6}$$

The emission e_λ and absorption spectra k_λ are then obtained for 5000 spectral points in the test cases presented in this work in a pre-set range from 305 nm to 320 nm.

The program simulates only the transitions of the $\mathrm{A}^2\Sigma^+ \rightarrow \mathrm{X}^2\Pi$ system and is set up to return the emission e_λ and absorption κ_λ spectra for the given conditions in the wavelength range of 305–320 nm. The transition band ($\nu = 0$, $\Delta\nu = 0$) was chosen following the approach of Stützer and Oschwald [47]. Experimental data were captured considering only this transition because transitions of higher orders had a too low signal-to-noise ratio. For the wavelength range, the 305–320 nm is chosen because at high pressures considered in this work, this is the range in which OH* radiation

---

[1] Points for sampling the thermodynamic properties can differ from the points that constitute a ray solution. A new set of points on the ray path can be arbitrarily generated through interpolation from a solution set of points

is more distinct and the central wavelength is 310 nm. The spectra can be calculated for a set number of equidistant spectral points [46]. The main transition is from the first electronically excited state to the ground state but the model includes a number of fine rotational vibrational transitions between the two electronic states. It also includes the effects of collisional broadening and Doppler broadening. The Einstein coefficients and spectroscopic constants are based on references [48–51].

Fig. 1 shows a sketch of the procedure. As the emission e_λ and absorption κ_λ spectra are obtained for the chosen points along the ray, the radiative transfer equation is solved for each wavelength starting from the physical origin of the ray in the chamber and towards the detector.

$$\frac{\mathrm{d}L_\lambda}{\mathrm{d}s} = e_\lambda(s) - \kappa_\lambda(s) \cdot L_\lambda(s) \tag{7}$$

In the above equation L_λ denotes the spectral radiance and s is the path length along the ray. Spectral radiance is multiplied with spectral transmittance $\tau_{\lambda,\text{filter}}$ of the OH* pass filter in order to make the results more comparable to the experimental measurements.

$$L_{\lambda,\text{filtered}}(s) = L_\lambda(s) \cdot \tau_{\lambda,\text{filter}} \tag{8}$$

Total filtered radiance L_{filtered} along the ray is obtained by integrating the spectral filtered radiance over the wavelength range 305–320 nm.

$$L_{\text{filtered}}(s) = \int_{305nm}^{320nm} L_{\lambda,\text{filtered}}(s)\mathrm{d}\lambda \tag{9}$$

With the previous steps a filtered total radiance is obtained for all the points along a single ray. For the creation of the pseudo-OH* images, only the radiance at the end of the ray is relevant, since this is the one detected by the sensor. It is assumed that the outgoing rays are detected with the same sensitivity, quantum efficiency and area.

3. Test case a: Fiala burner

The method described in Section 2 is applied to the test case described by Fiala [28], in which several flame visualization techniques have been applied. In his work, Fiala investigated three radiation models to compare OH* radiation observed in an experimental burner and the OH* radiation extracted from CFD simulations in order to determine if a quantitative correlation between heat release rate and OH* radiation intensity could be established. The three investigated models are the Detailed Chemistry model (DC), a Spectral Model (SM) and the Equilibrium Filtered Radiation Model (EFRM) developed by Fiala [28]. In the frame of this work, we will focus on the comparison between the SMART algorithm and the spectral model used by Fiala.

The main reason for this choice is the nature of both SMART and SM. In the SM, the emission spectra of OH is simulated on the basis of the HITRAN/HITEMP database, in which the list of individual lines at reference conditions, their wavenumbers, precalculated line intensities, and FWHM of the pressure broadening are tabulated. Then, a Python tool reconstructs the spectra up to the 3000 K. The SM takes into account self-absorption, which is not included in EFRM. SMART calculates the spectra of OH* with a radiation modelling program by Potter [46], and also takes into account self-absorption. As self-absorption in OH* imaging cannot be neglected as was concluded by Fiala when comparing to experiments, this is for sure an important parameter of choice in the models which can be directly compared. Fiala extended the EFRM model into EFRM-A to approximate the self-absorption while keeping the computational complexity low. Fiala states that SM needs to be employed to describe self-absorption in a physically correct way, but EFRM-A can be used to decide whether self-absorption is to be taken into account or is negligible, and compares the application and results of the EFRM-A, EFRM, SM and Detailed Chemistry model [52].

Both SM and SMART models take as input parameters OH molecules concentration and temperature and are applied in a post-processing step, unlike DC where OH* concentration is produced at run-time with an embedded chemical scheme. In order to compare radiation models, the choice of SM for comparison resulted to be straightforward, as the current implementation of SMART accounts for the molecule spectra when generating the pseudo-radiation images.

The flame studied by Fiala is a laminar hydrogen-oxygen flame, in which fuel and oxidizer are in gaseous state. Fig. 2 shows a sketch of the experiment and the ray paths starting from the pinhole camera to the quartz lenses rendered for the application of the ray tracing in SMART. Detailed information about the optical setup and measurement tools can be found in Ref.[28].

In Fiala's work [28], a CFD simulation with a detailed chemistry scheme was performed, considering the domain highlighted in green in Fig. 2(a). In a second step, both the EFRM (Equilibrium Filtered Radiation Model) and the SM (Spectral Modelling) were applied to the simulation results. A detailed explanation of the two models can be found in Fiala [28]. A study was carried out for all the chamber pressure conditions listed in Fiala [28], but here only two cases are presented, one at low pressure (1 bar) and one at higher pressure (30 bar), where the phenomenon of self-absorption cannot be neglected.

3.1. Results and discussion

First, the influence of the spectral modelling without refraction is investigated by comparing the results of the application of the SMART with line-of-sight (LOS) integration method using CFD results provided by Fiala [28]. The term LOS integration refers to the case where the refraction of the rays within the chamber volume is not considered. Thus, rays are taken as straight lines crossing the combustion media and consequently the radiative transfer Eq. (7) is integrated over a straight path. For SMART, the rays are generated projecting the image in the focal plane of the camera, which approximately coincides with the combustion chamber plane, as an external observer would see them. The displayed quantities correspond to the normalised OH* radiation between the minimum and maximum intensity values as collected by the camera. This comparison allows to estimate the influence of refraction. Fig. 3a and b show the results of LOS integration compared to SMART for both pressures of 1 bar and 30 bar, respectively.

The comparison shows that, for both cases, no substantial difference can be detected. This is not unexpected in this case, due to the combustion of propellants in a gaseous state, where the density gradients between oxygen and hydrogen streams are not large enough to give an important difference in terms of refraction index. The result in this case is that the inclusion of refraction is not a key point when dealing with gas-gas interfaces.

Subsequently, the SMART tool has been applied to Fiala's simulation results as a post-processing step, in the same way he did with the SM. Figs. 4 and 5 show the comparison between the SM and SMART, including plots which show the difference in radiation between the two methods at chamber pressure of 1 bar and 30 bar, respectively. Both methods account for self-absorption, but only SMART includes ray-tracing, whereas SM treats the radiance with LOS integration. SMART takes into account refraction with the rays trajectories displayed in Fig. 2(b).

As can be seen in the Figures, the two flame images show similar shapes. However, in the SM the volume of the flame is slightly wider than the one produced by SMART. Focusing on the length of the radiation zone, Fig. 4a shows a discrepancy of 5% at 1 bar and

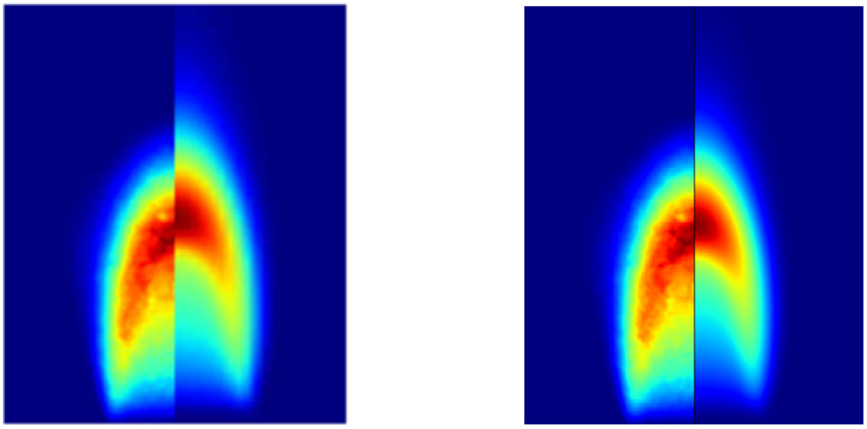

(a) Experiment (left) vs. Fiala SM (right) [28].

(b) Experiment (left) vs. SMART (right).

Fig. 6. Comparison of the experimental data with SM (a) and SMART (b) at the chamber pressure of 1 bar. The values of both plots are normalised with respect to the experimental values between 0 (blue) and 1 (red) to make a meaningful comparison. (For interpretation of the references to color in this figure legend, the reader is referred to the web version of this article.)

Fig. 5a discrepancy of 3% at 30 bar, which corresponds to 10 mm and 1 mm respectively. Figs. 4b and 5b show that the biggest difference in OH* radiation occurs in the zone where refraction index gradients are higher. For both cases, SMART presents a more compact flame with respect to SM, with a slight shift downstream of the radiation in the central zone near the injection plane, although the anchoring zone is slightly closer to the injection plane in SMART for the 30 bar case. Quantitative differences in radiation are shown in Figs. 4b and 5b. The highest difference can be seen in the outer zone of the flame, where SM gives a wider flame. Since it was shown in Fig. 3 that including refraction has negligible influence for a gas-gas laminar flame because the density gradients are too low, the difference is probably lying in the model used to generate OH* spectra and in the interpolation of the original CFD results on a different mesh used to apply SMART. Another source of discrepancy could be the source of generation of the rays: although special care was taken to produce the rays in the same way as described by Fiala [28], it was not possible to estimate how the refraction of the rays at the side quartz-windows and quartz lance was taken into account in the SM.

Lastly, a fundamental comparison for the validation of SMART has to be made against the experimental data provided by Fiala [28]. Figs. 6 and 7 show the experimental data compared with the results of SM and SMART at a chamber pressure of 1 bar and 30 bar, respectively.

In the SM model as noted by Fiala, the radiation produced by the application of the model has a peak which is shifted downstream with respect to the experimental image. Comparatively, in SMART a smaller flame volume for both 1 bar and 30 bar chamber pressure can be seen, and radiation peaks slightly upstream compared to SM, thus yielding a flame shape which is more similar to the experiment. The shifting in the length of the flame between the experiment and the SM leads to an overestimation of the latter of 11.8% at 1 bar and 47.6% at 30 bar, whereas the same quantity between the experiment and SMART amounts to 5.4% at 1 bar and 38.8% at 30 bar. According to Fiala, the downstream peak of SM results are a consequence of the CFD simulations. However, results from SMART show that in spite of using the same underlying data, the peak is observed slightly upstream, thus indicating that the modeling of radiation may as well contribute to this phenomenon. The Fiala test case showed that the application of SMART is successful for a laminar gas-gas flame under different pressure conditions. Because of the nature of the flame, there are no strong density gradients which cause important changes of the refraction index field. For gas-gas laminar flames a LOS integration is sufficient, but as a first test case the results of SMART are in slightly better agreement with experimental data than SM with respect to the peak radiation. The next step was to apply the SMART algorithm to a transcritical turbulent flame, which is presented in the next section.

4. Test case B: Optically accessible rocket combustor BKH

To test the application of the SMART routine, an experimental combustor with large optical access windows providing a view of five closely clustered flames was chosen. The combustor, designated BKH, is an experimental combustor developed by DLR Institute of Space Propulsion and operated at P8 test bench in Lampoldshausen [3]. The combustor has a rectangular cross section. It has a length of 305 mm, a width of 50 mm and height of 200 mm. BKH has five primary shear coaxial injectors fed with LOx-H_2 in a matrix pattern. Above and below are arrays of 50 secondary injectors fed with hydrogen.

BKH is equipped with an optical system which allows the flame to be investigated. Observation windows provide optical access to the near injection region. The windows on each side have a length of 100 mm and height of 50 mm. The quartz windows are cooled by hydrogen cooling film at ambient temperature. Images are acquired using a high-speed optical systems, including OH* imaging of the flame radiation. For the OH* imaging system, radiation passed through a filter with a peak of 305 nm and FWHM of 10 nm. Fig. 8 shows a sketch of BKH.

For the present study, the OH* high-speed images have 228x114 pixels, where each pixel is stored as a monochromatic value of 8 bits. The spatial resolution is 446 ± 22 μm/pixel.

4.1. Numerical modelling

The flame is investigated using a steady state simulation (RANS) under the prescribed operating conditions by Beinke [53]. The final step is the application of the SMART tool. The images obtained are then compared with the experimental data.

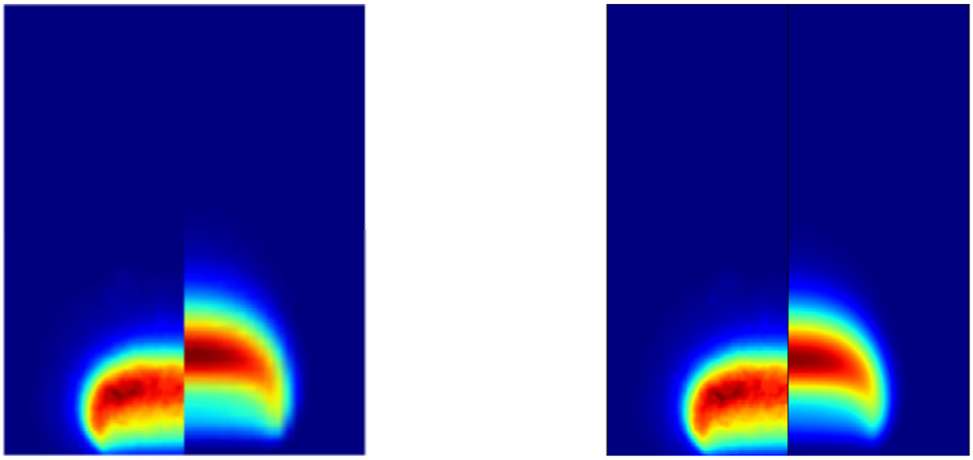

(a) Experiment (left) vs. Fiala SM (right) [28].

(b) Experiment (left) vs. SMART (right).

Fig. 7. Comparison of the experimental data with SM (a) and SMART (b) at the chamber pressure of 30 bar. The values of both plots are normalised with respect to the experimental values between 0 (blue) and 1 (red) to make a meaningful comparison. (For interpretation of the references to color in this figure legend, the reader is referred to the web version of this article.)

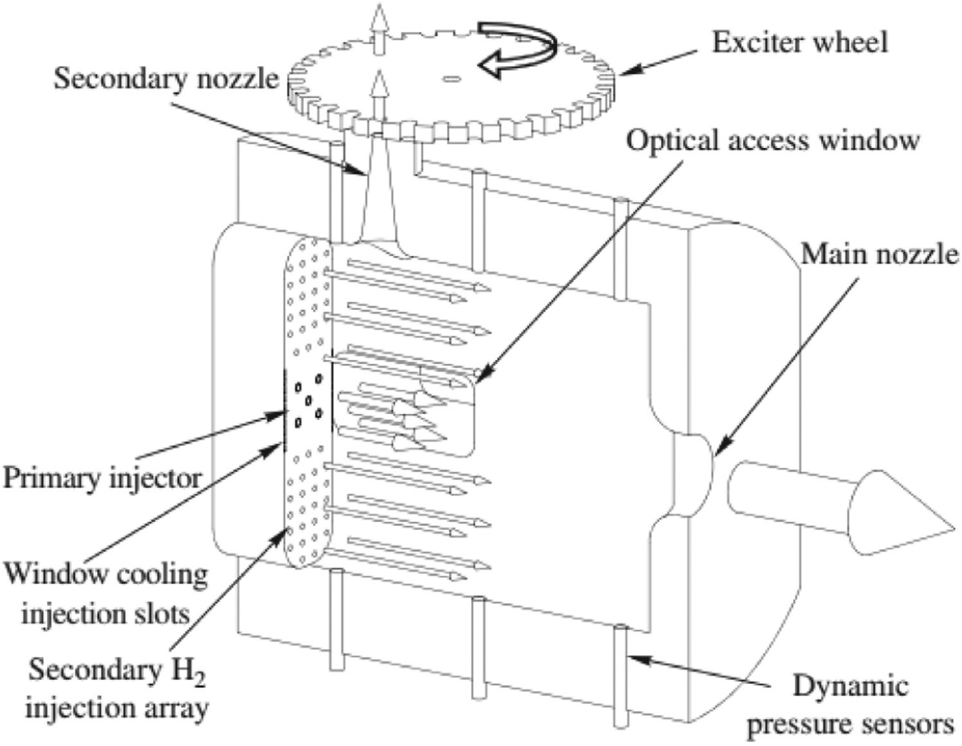

Fig. 8. BKH.

4.1.1. CFD Solver

The simulations are run using the DLR in-house code TAU. The DLR TAU code is a hybrid (structured/unstructured) grid Godunov-type finite-volume flow solver for the compressible Euler and Navier-Stokes equations. Spatial second order is reached by a MUSCL reconstruction. DLR TAU code has been validated for a range of steady and unsteady flow cases. Detailed information can be found in references [54–56]. The one equation Spalart-Allmaras turbulence model described in [57] was selected, a MAPS+ Riemann solver by Rossow [58] is used to handle low Mach number flows and high density gradients, which are challenging for a compressible flow solver. An explicit 3rd order Runge-Kutta scheme is used for time integration. A six-species and seven-step reaction scheme for oxygen-hydrogen combustion published by Gaffney et al [59] that includes the species H_2, O_2, H, O, OH and H_2O was employed. A more specific description of the setup of the simulation can be found in Beinke [53].

Cryogenic propellants at high pressures, as in rocket engines, behave differently than ideal gases and this has to be taken into account. These real-gas effects are included in the DLR TAU code real gas release to model the transcritical injection and combustion of cryogenic propellants. This real gas implementation has two

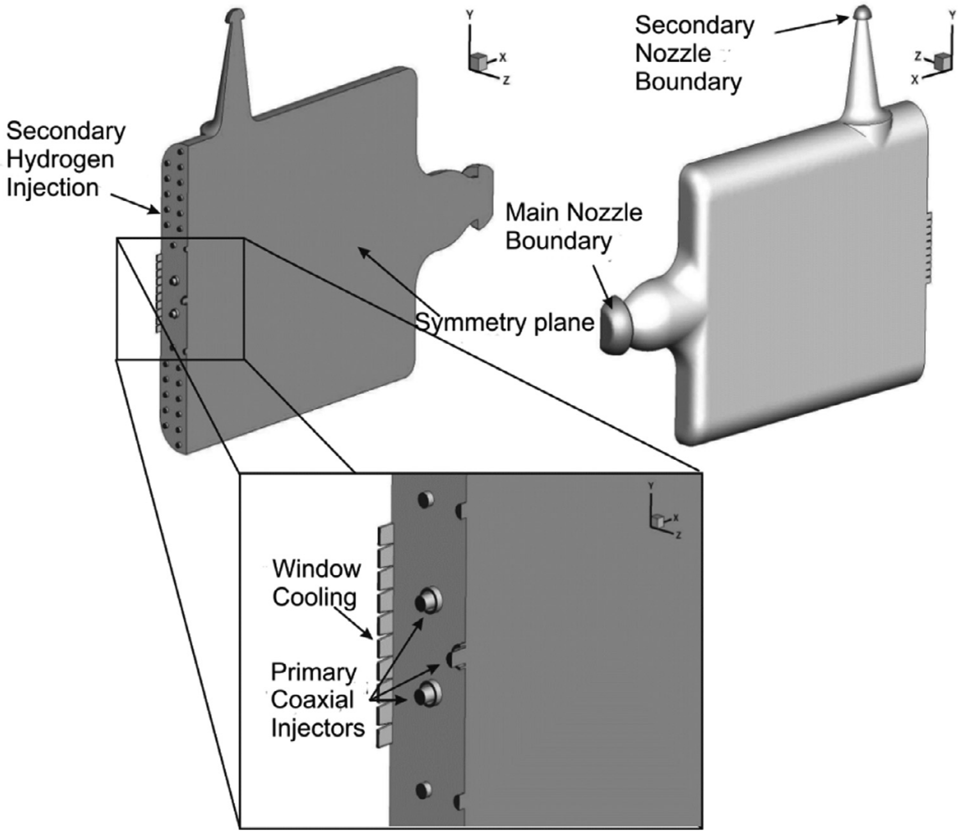

Fig. 9. Computational domain [53]

main features: each species has a dedicated equation of state and the properties of the mixture are determined by a multi-fluid mixing model, see [60–62]. Here the ideal gas equation of state is solved for H_2, H, O, OH and H_2O, and a real gas equation of state is solved for O_2. The real gas properties of oxygen are computed from the high fidelity modified Benedict-Webb-Rubin (MBWR) equation of state (EOS) of Younglove [63] and stored in a library during a pre-processing step. Thermodynamic state variables, such as pressure, enthalpy, heat capacities, speed of sound, etc. are all computed consistently from the real gas EOS. Real gas corrections to the transport coefficients are evaluated following Lemmon and Jacobsen [64]. The implemented multi-fluid mixing model assumes ideal mixing of species properties. This is only valid if all species exist as a real-gas in only a pure-fluid state. However, this assumption is physically justified in this work focused on supercritical oxygen-hydrogen combustion. Banuti et al. [60,65] explain that, for oxygen-hydrogen combustion at supercritical pressures, the LOx transitions from a liquid to a supercritical gas-like state under pure fluid conditions, where essentially all real fluid effects are confined to the LOx core. Thus, for the flames considered in the present work, the multi-fluid ideal-mixing model is appropriate. The fluid in the numerical domain is assumed to exist as either a pure-fluid real-gas or a mixture that can be approximated using an ideal-mixing model. The fluid is treated as a continuous Eulerian mixture with no discrete phases or phase changes. This approach is sometimes referred to as an Euler-Euler model.

4.2. Results

The simulation of BKH was performed by Beinke [53]. Fig. 9 shows the simulation domain. The domain features the rectangular chamber volume and both the main and secondary nozzles. BKH has a vertical symmetry and so the modeled domain consists in half of the chamber to reduce the size of the computational domain and consequently the computational costs.

Fig. 10 shows the mesh used for the calculations. A fully unstructured mesh is used to simplify mesh development and better adapt to the complex geometry of the chamber and has approximately 2.6 M nodes.

A detailed description of the simulation results is out of the scope of this work. More information can be found in Beinke [53]. Fig. 11 shows the distribution of the variables used in SMART to derive the pseudo-OH* images. SMART is applied in this case to a time averaged image and so the fluctuations of the variables used as an input for the algorithm are not captured. However, the focus of this work is on the SMART algorithm and not on the CFD model of BKH. For that reason, a rather simple RANS solution was chosen. Nevertheless, the SMART approach is generally applicable and can also be applied to unsteady high-fidelity CFD result.

Fig. 12 provides insights on how and at which location rays are refracted. It is important to note that only the rays that exit the chamber perpendicular to the window surface are considered, as depicted in Fig. 1. This is possible because of the large distance between the camera and the window. In fact, the solid angle of each pixel is negligible and therefore the assumption of parallel rays is acceptable. However, SMART also allows to take into account incoming rays from different directions. In other experiments it is clear that also rays which are not parallel to the optical axis of the windows can play a role.

The color of the rays corresponds to the integrated total radiance, the thickness of the rays to the areas where larger emission occurs. Rays are bent where the LOx cores present density gradients. The rays are attenuated when they pass through the OH-rich reacting shear layer on the other side of the core. However, our model does not account for any absorption, scattering or internal refraction inside the LOX jet itself. It can be also seen that the total

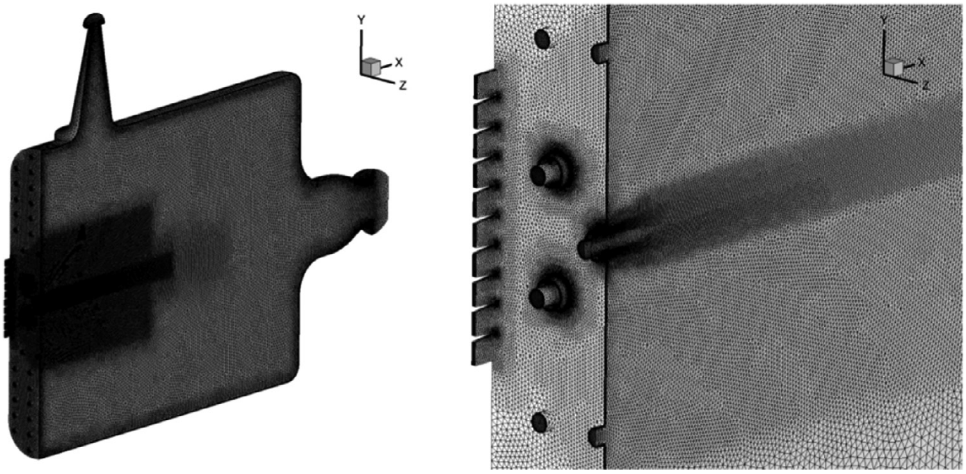

Fig. 10. Mesh with detail in near injection region [53].

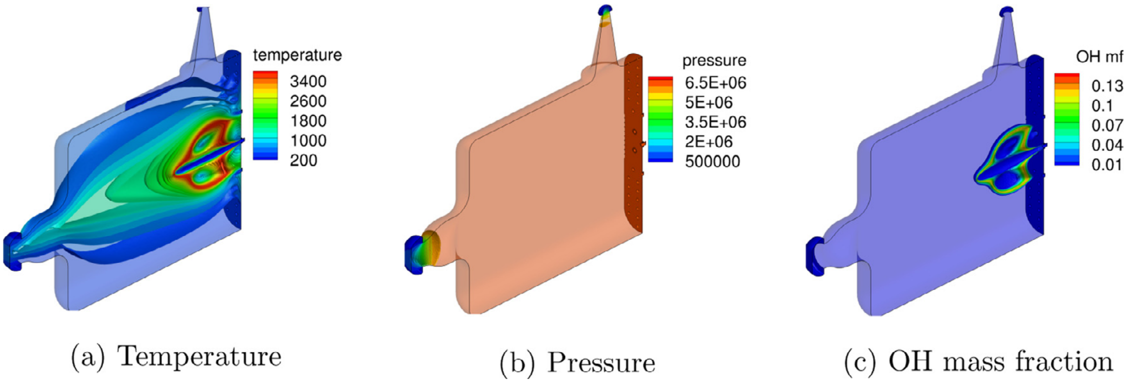

(a) Temperature (b) Pressure (c) OH mass fraction

Fig. 11. Temperature (a), pressure (b) and OH mass fraction distribution (c) in BKH. The load point refers to 60 bar chamber pressure and ratio oxidizer to fuel (ROF) 6 [53]. These distributions are used as an input for the ray tracing algorithm which generates the pseudo-OH* images.

radiance of a ray changes significantly only if the ray is refracted in such a way that it passes tangentially through the shear layer where there is presence of OH*. Fig. 13 compare the experimental image with the 1D integrated image of OH* concentration from Beinke [53], where the colormap has been adjusted to have better comparison, and the fully ray-traced image obtained with SMART, respectively.

Some important observations can be done comparing the two simulation results with the experimental data shown in Fig. 13a. As already stated by Beinke [53], the most important difference between experiments and simulation in the frame of this work is that the OH distribution does not extend until $x = 100$ mm, which corresponds to the end of the window in the steady-state model. The OH distribution ends slightly downstream of the oxygen jets and this indicates that the oxygen is consumed too rapidly in the simulation. However, it could be also due to the fact that the transport of OH* molecules is not taken into account. This still holds true because OH* molecules are a subset of OH ground state molecules, and a detailed description of OH* production is not modeled in the chemistry scheme adopted for the simulations. The absence of modeling the OH* transport could cause then the underestimation of radiation close to the end of the window at $x=$ 100 mm.

With respect to the EFRM model of Fiala [28] as it was applied by Beinke in previous simulations [53], the self-absorption is now correctly taken into account and the emission is spectrally resolved and not assumed to originate from a single transition at a specific wavelength. The integrated spectral radiance L_λ is also multiplied for the spectral transmittance of the filter $\tau_{\lambda, filter}$, which attenuates the spectral radiance values according to their wavelength. Moreover, a fully three dimensional ray tracing allows the visualization of high density regions of the LOx cores according to the physical mechanisms of refraction. Nevertheless, the comparison of the optical data and simulations is still not satisfactory.

4.3. Discussion

The spectral modelling script described in Section 2 simulates the emission and absorption spectra from the thermal excitation of OH molecules. Chemiluminescense is neglected because thermal excitation is the main source of excitation. Fig. 14 shows several physical parameters along a chosen ray path which help to have further insights about where emission occurs under rocket combustion chambers operating conditions and refers to the algorithm applied to the BKH CFD solution. The main reason of increased flame emission are high temperatures and the presence of OH molecules. The considered ray passes through two LOx jets, which can be observed in the two sections where temperature drops between 10 and 16 mm and 34 and 38.5 mm along the ray path. In the second one, the ray passes through the center of the jet where the temperature is cryogenic. Four zones of emission, highlighted in red, can be observed. The total radiance along the ray path shows a fluctuating behavior where thermal excitation occurs, with a slight spatial delay.

It is difficult to state when the total radiance changes because its values are obtained using the contributions of spectral radiance at different wavelengths, where Eq. (7) is solved. The equations shows that when absorption has a greater effect than emission, then the spectral radiance must be high as well as the absorption

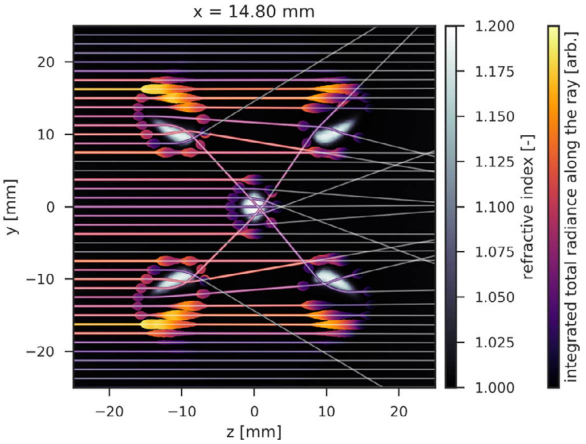

(a) Ray paths at x=14.8 mm

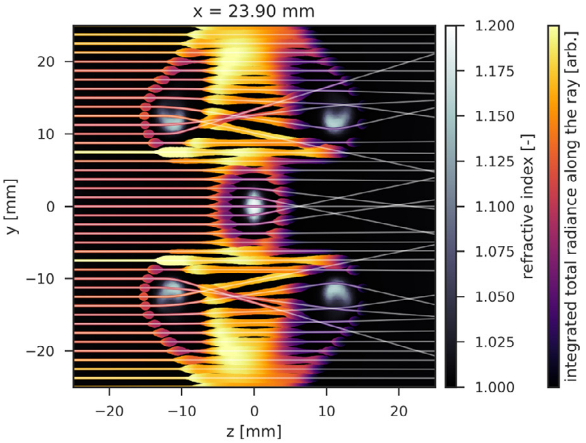

(b) Ray paths at x=23.9 mm

Fig. 12. Ray paths visualization through refractive index gradients corresponding to the increasing density of the LOx jet at different locations.

coefficients. Self-absorption has then an important effect at the operating conditions of rocket combustion chambers and affects the flame emission. The integrated radiance has to be obtained first for each wavelength line-by-line, because self-absorption has a larger effect at wavelengths where emissivity is high and relatively small where emissivity is low. Fig. 15a shows the difference in terms of radiance solving Eq. (7) with and without self-absorption. Figure 15b shows the over prediction of radiance with respect to the final result. Neglecting self-absorption would produce an over estimation of radiance with a factor of 15 for rays passing through multiple flames before reaching the observer.

It is crucial to consider also the inclusion of the refraction effects in the simulation algorithm. Fig. 16 shows the relative difference of the radiance on a pixel-by-pixel level between a fully ray traced image and a 1D integrated image which does not include refraction.

It is observed that the largest difference lies between x=0 and x=20 mm, just downstream the injection plane, where hydrogen and oxygen streams interact, and at the edge of the recirculation zones which are generated from the secondary hydrogen injection, where the density gradients between the two streams are higher. This indicates that it is important to take refraction into account in flames with liquid-gas interfaces in order to produce a pseudo-OH* image which correctly captures its influence, which is experimentally captured by the camera. It allows to have a more correct comparison between the CFD simulation results and the experimental images.

The advantages of using SMART are not clearly visible in the application to the Fiala test case due to the nature of the investigated

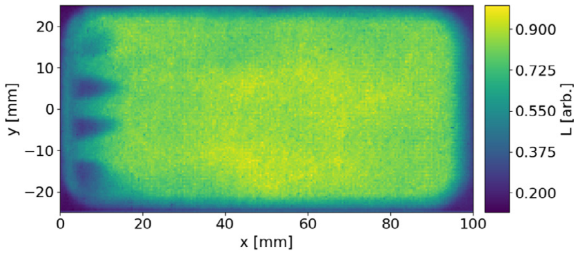

(a) Time averaged OH* radiation measurements

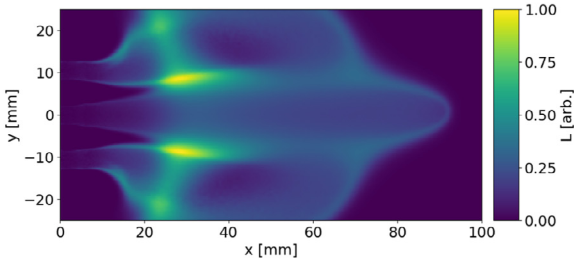

(b) 1D Integrated [OH]* [53]

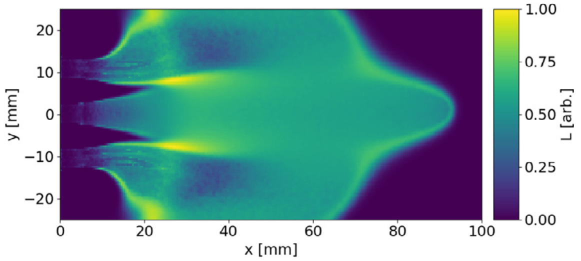

(c) SMART

Fig. 13. Comparison between the time averaged OH* radiation measurements (a), the LOS integrated image [53] (b) and the image obtained with SMART (c).

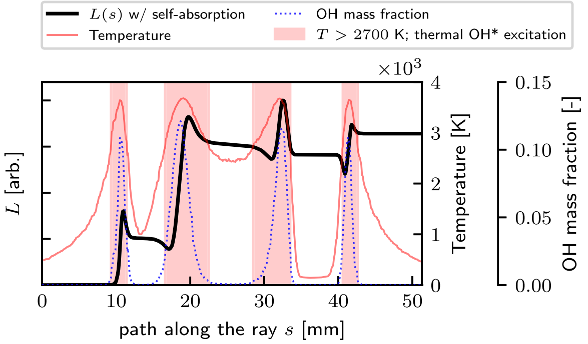

Fig. 14. Integrated radiance along the ray path. The regions where thermal excitation occurs are marked with red boxes. They coincide with the zones of OH* presence. (For interpretation of the references to color in this figure legend, the reader is referred to the web version of this article.)

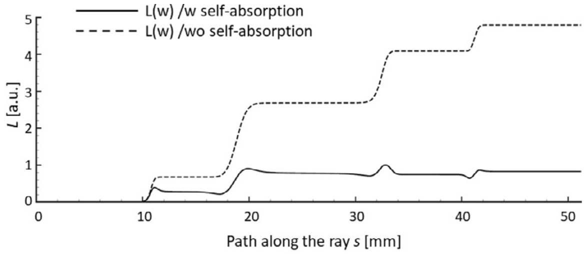

(a) Ray radiance along the ray path with and without self-absorption.

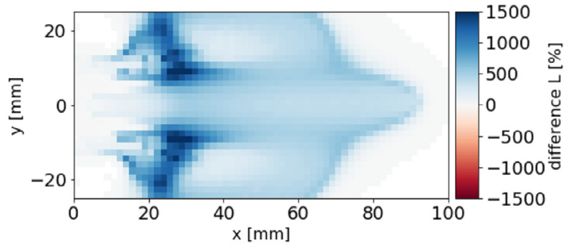

(b) Relative overprediction of total radiance for each pixel neglecting self-absorption.

Fig. 15. Difference in radiance prediction with and without self absorption.

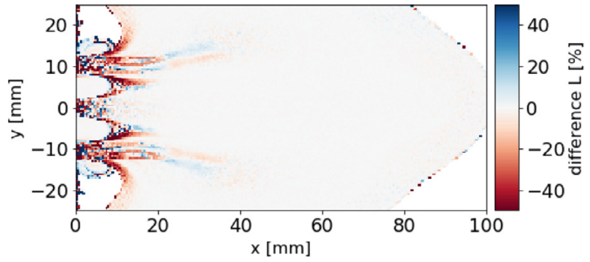

Fig. 16. Relative difference in simulated total radiance between fully ray traced and 1D integrated image. The values are normalised to the pixel values of the 1D integrated image.

flame itself. However, looking at the BKH case, it is crucial to include both ray-tracing and self-absorption because of the presence of strong density gradients, and then of refraction.

5. LES simulation of test case B

In order to test the application of SMART on a simulation, a LES simulation of test case B by Morii et al. [40] was employed. With this simulation, the effects of a more accurate turbulence model on the CFD simulation have been taken into account and it was possible to verify if this has an impact on the extension of the OH field and therefore on the OH* radiation itself, as it is considered a subset of the OH molecules. This simulation has the same operating parameters of the RANS, and the considered fields are time averaged in order to obtain a distribution comparable to the experimental data. A flamelet model is used for the turbulent combustion model, and the detailed chemical reaction model with 8 species including OH were used to create the flamelet table. The domain of the LES simulation is a full 3D geometry with five coaxial injectors, as shown in Fig. 17.

Fig. 18 shows a cut at the center plane of the OH mass fraction and temperature field on which SMART is applied. The maximum temperature value reached in the simulation is about 3500 K.

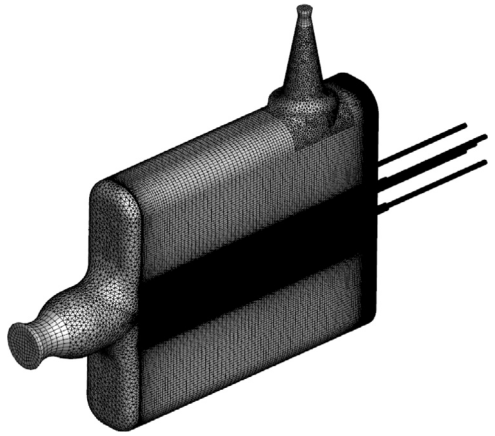

Fig. 17. Domain and mesh of the LES simulation used for the test of SMART of higher order simulation. The mesh is hybrid, with a structured part in the chamber volume, injectors and divergent part of the nozzles and unstructured in the convergent part of nozzles and at the base of them.

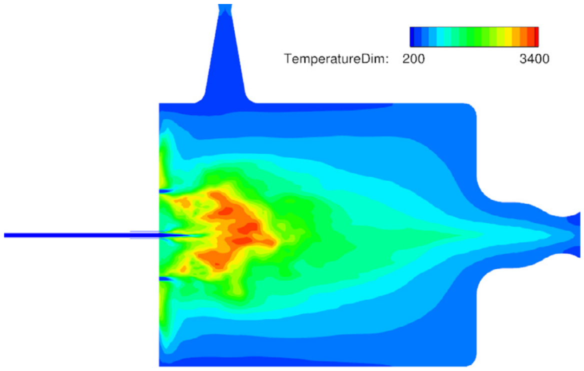

(a) Temperature field

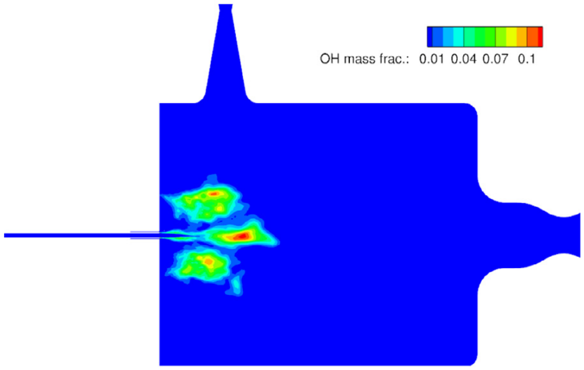

(b) OH mass fraction field

Fig. 18. Temperature and OH mass fraction distribution at the center plane of the LES simulation. The distributions are time averaged.

As it can be seen from the temperature and OH fields, also in the LES simulation the flame does not extend downstream until the end of the window.

SMART was applied to the results of the LES simulation over an area corresponding to the window edges. In order to test the routine, 5000 rays were generated, with a pixel size of 2x2 mm. The required computational time on a single core was about 200 CPU hours. The domain was reduced before the application of the algorithm to an area corresponding to the camera view. Fig. 19 shows the post-processed image after the application of SMART and the

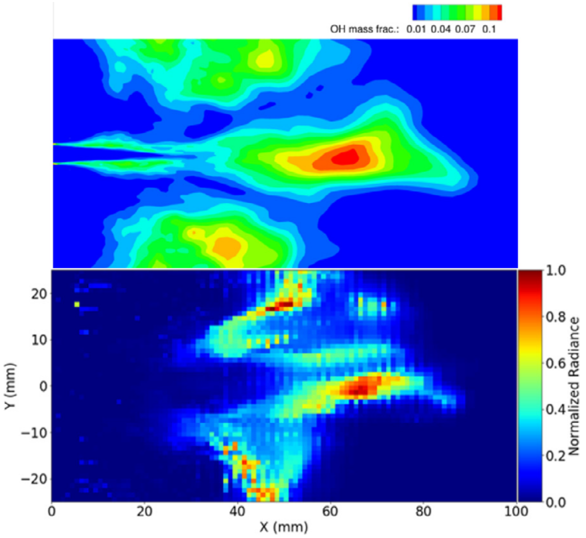

Fig. 19. Comparison of the OH mass fraction distribution in the window region of the LES simulation and the application of SMART in the same area. In the regions where the OH mass fraction has a higher value, the radiance is considerably higher. The values are of the radiance are normalized between 0 (blue) and 1 (red). (For interpretation of the references to color in this figure legend, the reader is referred to the web version of this article.)

OH field zoomed in the window area obtained by the CFD simulation.

From the comparison, it can be seen that in zones where the OH mass fraction is more abundant, the normalized radiation is more intense, reaching the maximum value. However, the regions when the temperature is relatively low are not visible in the radiance simulation. This is because chemiluminescence has to be taken into account at run time, where the production of OH* is modeled with a detailed chemistry scheme, whereas SMART acts as a post-processing tool to give the intensity of the thermal radiation of the flame. In regions where the temperature is lower, chemiluminescence plays a role also for high pressure conditions and this is outside the scope of SMART, gives an estimation of the total thermal radiation coming from the high temperature flame zone for thermally excited OH. Chemiluminescence should be modelled in the CFD simulation, and then be taken into account to provide an estimation of the total OH* radiance of the flame.

6. Conclusions and outlook

A method for comparing CFD results and optical measurement of filtered radiation from high pressure oxygen hydrogen flames was developed. Pseudo-OH* images are generated from the CFD simulation solutions. The SMART post-processing routine which produces the images first performs reverse ray-tracing from each pixel of the image, sampling the thermodynamic properties along the path and modelling the emission and absorption spectra for wavelengths between 305 and 320 nm. Then the spectral radiance along the ray is obtained by solving the radiative transfer equation line-by-line. Finally, the spectral radiance is integrated to obtain the total radiance.

The comparison with the previous work of Fiala shows a slight improvement in the match with experimental data with respect to the SM model he adopted, pointing out that also the spectral model used has an impact on the solution and not only the data produced by the CFD simulation, also if they still remain the basis for this kind of approach which is applied in a post-processing step. Nevertheless, in a laminar gas-gas flame there is no big difference between the results with and without refraction, as it could be expected due to the relatively small density gradients in the combustion chamber.

Density gradients and therefore the impact of refraction become important cryogenic flames such as those in the second experimental test case addressed with the SMART routine in this work. In previous works, neglecting self-absorption, the total radiance is overpredicted by a factor of 15 in the multi-flame rocket combustor test case considered here. The use of ray-tracing, which models the refraction of the light as it passes through the chamber, has a significant effect, especially for rays interacting with the LOx jet, as refraction in these zones can be very high. Comparing the experimental images with the ones produced by the current method, the difference is still significant but lies in the ability of the CFD solver to predict the distribution of OH* partial density in the field of view of the combustor. Concerning the turbulence model used, no relevant difference is shown comparing the results of RANS and LES flamelet simulation, showing that in this case the turbulence model used does not impact significantly on the final results, although the LES simulation gives more details about the turbulent structures in the solution.

Comparing LOS integrated images with fully ray-traced ones, the absolute difference in radiance reaches about 20% of the normalized image radiance range. In regions where rays encounter the LOx jets, rays gathering radiance by passing through multiple flames are shown to be just as bright as those passing through only one, due to self-absorption.

SMART takes into account two very important phenomena contributing to the flame radiance, which are refraction and self-absorption. This allows to reduce the overprediction of the flame radiation for a more accurate relative intensity distribution in a pseudo-OH* image. The comparison with experimental data is improved, allowing better validation of CFD models using experimental data from flame visualization. However, the analysis also indicated that for better validation of OH* flame visualization between experiments and CFD, a chemiluminescence model should be considered in the CFD simulations in the future.

Declaration of Competing Interest

The authors declare that they have no known competing financial interests or personal relationships that could have appeared to influence the work reported in this paper.

Acknowledgments

I would like to thank Dr. Thomas Fiala for giving permissions to use data from his doctoral thesis to perform comparisons with the SMART results and for answering our questions, and Dr. Scott Kenneth Beinke for the simulation data used to apply SMART to BKH.

Supplementary material

Supplementary material associated with this article can be found, in the online version, at doi:10.1016/j.combustflame.2021.111614.

References

[1] M.J. Bedard, T.L. Fuller, S. Sardeshmukh, W.E. Anderson, Chemiluminescence as a diagnostic in studying combustion instability in a practical combustor, Combust. Flame 213 (2020) 211–225.

[2] S. Sardeshmukh, M. Bedard, W. Anderson, The use of OH* and CH* as heat release markers in combustion dynamics, Int. J. Spray Combust. Dyn. 9 (4) (2017) 409–423.

[3] J.S. Hardi, Experimental Investigation of High Frequency Combustion Instability in Cryogenic Oxygen-Hydrogen Rocket Engines, University of Adelaide, Australia, 2012 Ph.D. thesis.

[4] J.C. Sisco, Measurement and Analysis of an Unstable Model Rocket Combustor, Purdue University, 2007 Ph.D. thesis.

[5] Test case rcm-3 mascotte single injector -60 bar-(2001).

[6] A.G. Gaydon, The Spectroscopy of Flames, second ed., Springer, 1974.

[7] R. Mavrodineau, H. Boiteaux, Flame Spectroscopy, Wiley, 1965.

[8] R.B. Price, L.R. Hurle, T.M. Sugden, Optical studies of the generation of noise in turbulent flames, Symp. Combust. 12 (1) (1969) 1093–1102.

[9] B. Hornstein, C. Budnik, W. Courtney, Research Study of Light Emission Caused by Pressure Fluctuations in Rocket Engines, Final Report, AFOSR, 1966.

[10] T. Katrothia, U. Riedel, A. Seipel, K. Moshammer, Experimental and numerical study of chemiluminescent species in low-pressure flames, Appl. Phys. 107 (B) (2012) 571–584.

[11] H. Najm, P. Paul, C. Mueller, P. Wyckoff, On the adequacy of certain experimental observable as measurement of flame burning rate, Combust. Flame 113 (1998) 312–332.

[12] M.A.A. Clyne, B.A. Thrush, Mechanism of chemiluminescent combination reactions involving oxygen atoms, Proc. R. Soc. Lond. Ser. A Math. Phys. Sci. 269 (1338) (1962) 404–418.

[13] G.P. Smith, J. Luque, C. C.Park, J.B. Jeffries, D.R. Crosley, Low pressure flame determination of rate constants for OH(a) and CH(a) chemiliminescence, Combust. Flame 131 (2008) 59–69.

[14] S.A. Farhat, W.B. Ng, Y. Zhang, Chemiluminescent emission measurement of a diffusion flame jet in a loudspeaker induced standing wave, Fuel 84 (14–15) (2005) 1760–1767, doi:10.1016/j.fuel.2005.03.020.

[15] E. Freitag, H. Konle, M. Lauer, C. Hirsch, T. Sattelmayer, Pressure influence on the flame transfer function of a premixed swirling flame, Turbo Expo 1 (2006) 477–486.

[16] M. Lauer, T. Sattelmayer, On the adequacy of chemiluminescence as a measure for heat release in turbulent flames with mixture gradients, Turbo Expo 2 (2009) 535–544, doi:10.1115/GT2009-59631.

[17] Y. Hardalupas, M. Orain, Local measurements of the time-dependent heat release rate and equivalence ratio using chemiluminescent emission from a flame, Combust. Flame 139 (2004) 188–207, doi:10.1016/j.combustflame.2004.08.003.

[18] J.G. Lee, A.D. Santavicca, Experimental diagnostics for the study of combustion instabilities in lean premixed combustors, J. Propul. Power 19 (5) (2003) 735–750.

[19] H. Wasle, A. Winkler, M. Lauer, T. Sattelmayer, Combustion noise modeling using chemiluminescence data as indicator for the heat release distribution, Eur. Combust. Meet. (2007).

[20] M. Wierman, N. Nugent, W. Anderson, Combustion response of a lox/lch4 element to transverse instabilites., 47th AIAA/ASME/SAE/ASEE Joint Propulsion Conference & Exhibit, American Insitute of Aeronautics and Astronautics (2011).

[21] T. Katrothia, I.U. Riedel, J. Warnatz, A numerical study on the relation of OH^*, CH^* and $C_2{}^*$ chemiluminescence and heat release, Proc. Eur. Combust. Meet. (2009).

[22] L.C. Haber, U. Vandsburger, W.R. Saunders, V.K. Khanna, An experimental examination of the relationship between chemiluminescent light emissions and heat-Release rate under non adiabatic conditions, Proce. IGTI (2000-NaN-121) (2000).

[23] F. Zhang, T. Zirwes, P. Habisreuther, H. Bockhom, A dns analysis of the correlation of heat release with chemiluminescence emissions in turbulent combustion, High Perform. Comput. Sci. Eng.'16 (2016) 229–243.

[24] T. Kathrothia, M. Fikri, M. Bozkurt, M. Hartmann, U. Riedel, C. Schulz, Study of the $H + O + M$ reaction forming OH^*: kinetics of OH^* chemiluminescence in hydrogen combustion systems, Combust. Flame 157 (7) (2010) 1261–1273.

[25] M. De Leo, A. Saveliev, L.A. Kennedy, S.A. Zelepouga, Oh and Ch luminescence in opposed flow methane oxy-flames, Combust. Flame 149 (4) (2007) 435–447.

[26] Y. Hidaka, S. Takahashi, H. Kawano, M. Suga, W.C. Gardiner, Shock-tube measurement of the rate constant for excited $OH(A2\Sigma^+)$ formation in the hydrogen-oxygen reaction, J. Phys. Chem 86 (8) (1982) 1429–1433, doi:10.1021/j100397a043.

[27] T. Koike, K. Morinaga, Further studies of the rate constant for chemical excitation of oh in shock waves, Bull. Chem. Soc. Jpn. 55 (1) (1982) 52–54.

[28] T. Fiala, Radiation From High Pressure Hydrogen-Oxygen Flames and its use in Assessing Rocket Combustion Instability, Technische Universität München, 2015 Ph.D. thesis.

[29] W.C. Gardiner, K. Morinaga, D.L. Ripley, T. Takeyama, Shock-tube study of OH (2Σ-2Π) luminescence, Phys. Fluids 12 (5) (1969), doi:10.1063/1.1692590. I–120–I–124

[30] M.C. Burrows, Radiation processes related to oxygen-hydrogen combustion at high pressures, Symp. Combust. (1965) 207–215.

[31] M. Zhao, D. Buttsworth, R. Choudhury, Experimental and numerical study of OH^* chemiluminescence in hydrogen diffusion flames, Combust. Flame 197 (2018) 369–377.

[32] Y. Liu, J. Tan, M. Wan, L. Zhang, X. Yao, Quantitative measurement of OH^* and CH^* chemiluminescence in jet diffusion flames, ACS Omega 5 (26) (2020) 15922–15930.

[33] H. Sheikhani, H. Ajam, M. Ghazikhani, A review of flame radiation research from the perspective of factors affecting the flame radiation, measurements and modeling, Eur. Phys. J. Plus 135 (343) (2020).

[34] H.R. Baum, W.E. Mel, Radiation and velocity fields induced by localized temperature fluctuations, Proc. Combust. Inst. 28 (2000) 473–479.

[35] M. Modest, Radiative Heat Transfer, third ed., Elsevier, Amsterdam, 2013.

[36] W. Malalasekera, H.K. Versteeg, J.C. Henson, J.C. Jones, Calculation of radiative heat transfer in combustion systems, Clean Air 3 (1) (2002) 113–143.

[37] X.L. Zhu, J.P. Gore, Radiation effects on combustion and pollutant emission of high-pressure opposed flow methane/air diffusion flames, Combust. Flame 141 (1–2) (2005) 118–130.

[38] X.L. Zhu, J.P. Gore, A.N. Karpetis, R.S. Barlow, The effects of self-absorption of radiation on an opposed flow partially premixed flame, Combust. Flame 129 (3) (2002) 342–345.

[39] S. Webster, J. Hardi, M. Oschwald, Comparison of oxygen-hydrogen combustion visualization techniques under representative conditions, Space Propuls. Conf. (2016).

[40] Y. Morii, S. Beinke, J. Hardi, T. Shimizu, H. Kawashima, M. Oschwald, Dense core response to forced acoustic fields in oxygen-hydrogen rocket flames, Propul. Power Res. 9 (3) (2020) 197–215.

[41] J. Perovšek, Ray Tracing and Spectral Modeling of Excited Hydroxyl Radiation from Cryogenic Flames in Rocket Combustion Chambers, LuleåUniversity of Technology, Department of Computer Science, Electrical and Space Engineering, 2018.

[42] A.M. Smith, M. Goldberg, E.S.K. Liu, Numerical ray tracing in media involving continuous and discrete refractive boundaries, Utrasonic Imaging (1980).

[43] J.H. Gladstone, T.P. Dale, XIV. Researches on the refraction, dispersion, and sensitiveness of liquids, Philos. Trans. R. Soc. Lond. 153 (1863) 317–343, doi:10.1098/rstl.1863.0014.

[44] M. Born, E. Wolf, Principles of Optics: Electromagnetic Theory of Propagation, Interference and Diffraction of Light, seventh ed., Cambridge University Press, 1999.

[45] J.R. Dormand, P.J. Prince, A family of embedded Runge-Kutta formulae, J. Comput. Appl. Math. 6 (1) (1980) 19–26.

[46] D. Potter, Modelling of radiating shock layers for atmospheric entry at Earth and Mars, School of Mechanical and Mining Engineering, The University of Queensland., 2011 Ph.D. thesis.

[47] R. Stützer, M.Oschwald, he hyperfine structure of the oh^* emission spectrum and its benefits for combustion analysis, Proceedings of the 8th European Conference for Aeronautics and Space Sciences EUCASS (2019).

[48] Lifbase, Accessed 21 July 2018, (https://www.sri.com/engage/products-solutions/lifbase).

[49] K. Huber, G. Herzberg, Molecular Spectra and Molecular Structure – 4. Constants of Dynamic Molecules, 4, Van Nostrand Reinhold, New York, 1979.

[50] J. Luque, D.R. Crosley, Transition probabilities in the $A2\Sigma^+$ - $X2\ \Pi_i$ electronic system of OH, J. Chem. Phys. 109 (2) (1998) 439–448.

[51] B. Ruscic, A.F. Wagner, L.B. Harding, R.L. Asher, D. Feller, D.A. Dixon, K.A. Peterson, Y. Song, X. Qian, C.-Y. Ng, et al., On the enthalpy of formation of hydroxyl radical and gas-phase bond dissociation energies of water and hydroxyl, J. Phys. Chem. A 106 (11) (2002) 2727–2747.

[52] T. Fiala, T. Sattelmayer, Assessment of existing and new modeling strategies for the simulation of OH^* radiation in high-temperature flames, CEAS Space J. 8 (1) (2016) 47–58.

[53] S.K. Beinke, Analysis of Flame Response to Acoustic Forcing in a Rocket Combustor, University of Adelaide, Australia, 2017 Ph.D. thesis.

[54] T. Gerhold, M. Galle, O. Friedrich, J. Evans, Calculation of complex three-dimensional configurations employing the DLR TAU code, 35th Aerospace Sciences Meeting and Exhibit, 1997, doi:10.2514/6.1997-167.

[55] A. Mack, V. Hannemann, Validation of the unstructured DLR-TAU-Code for hypersonic flows, 32nd AIAA Fluid Dynamics Conference and Exhibit (2002), doi:10.2514/6.2002-3111.

[56] D. Schwamborn, T. Gerhold, V. Hannemann, On the validation of the DLR-TAU code, New Results in Numerical and Experimental Fluid Mechanics (1999), pp. 426–433. Notes on Numerical Fluid Mechanics

[57] P.R. Spalart, S.R. Allmaras, A one-equation turbulence model for aerodynamic flows, 30th Aerospace Sciences Meeting and Exhibit, Aerospace Science Meeting, 1992.

[58] C.-C. Rossow, Extension of a compressible code toward the incomproessible limit, AIAA J. 41 (2003) 2379–2386.

[59] R. Gaffney, J.A. White, S.S. Girinaji, P. Drummond, Modeling turbulent/chemistry interactions using assumed pdf methods, AIAA/SAE/ASME/ASEE Joint Propulsion Conference and Exhibit (1992).

[60] D. Banuti, Thermodynamic Analysis and Numerical Modeling of Supercritical Injection, University of Stuttgart, 2015 Ph.D. thesis.

[61] D. Banuti, K. Hannemann, Efficient multiphase rocket propellant injection model with high quality equation of state, Proceedings of the 4th Space Propulsion Conference (2014).

[62] D.T. Banuti, V. Hannemann, K. Hannemann, B. Weigand, An efficient multi-fluid mixing model for real gas reacting flows in liquid propellant rocket engines, Combust. Flame (168) (2016) 98–112.

[63] B.A. Younglove, Thermophysical properties of fluids. 1.argon,ethylene,parahydrogen,nitrogen,nitrogen trifluoride and oxygen, J. Phys. Chem. Ref. Data (11) (1982).

[64] E. Lemmon, R. Jacobsen, Viscosity and thermal conductivity equations for nitrogen, oxygen, argon, and air, Int. J. Thermophys. (2004).

[65] D. D.Banuti, P.C. Ma, J.-P. Hickey, M. Ihme, Sub- or supercritical? a flamelet analysis for high-pressure rocket propellant injection, 52nd AIAA/SAE/ASEE Joint Propulsion Conference, volume AIAA-2016-4789, Salt Lake City, UT (2016).